Design and Performance Characteristics of the New 8.5-m Dual-Offset Gregorian Antenna for the CSU–CHILL Radar

V. N. BRINGI

Colorado State University, Fort Collins, Colorado

R. HOFERER

GDSATCOM, Kilgore, Texas

D. A. BRUNKOW

Colorado State University, Fort Collins, Colorado

R. SCHWERDTFEGER

GDSATCOM, Kilgore, Texas

V. CHANDRASEKAR, S. A. RUTLEDGE, J. GEORGE, AND P. C. KENNEDY

Colorado State University, Fort Collins, Colorado

(Manuscript received 12 May 2010, in final form 14 March 2011)

ABSTRACT

The Colorado State University–University of Chicago–Illinois State Water Survey (CSU–CHILL) national weather radar facility has been operated by the Colorado State University under a cooperative agreement with the U.S. National Science Foundation from 1990 to the present. The radar is configured to measure the elements of the 3×3 polarimetric covariance matrix based on using a two-transmitter and two-receiver system in the horizontal–vertical polarization basis. This S-band Doppler, dual-polarized radar facility is used for observations of precipitation with the highest possible data quality. To achieve this, a new dual-offset 8.5-m Gregorian antenna was custom designed and built by VertexRSI (now General Dynamics SATCOM) in Kilgore, Texas, to replace the circa 1994 center-fed parabolic reflector antenna. Here, the design features used to achieve the stringent specifications in terms of the sidelobe envelope and off-axis cross-polar levels are described, and the way in which they were validated at the manufacturer's long- and short-range pattern measurement facility.

Measurements in several different storm types, including stratiform rain and an intense hailstorm, and ground clutter (from mountains) are used to illustrate the new antenna performance. The linear depolarization ratio (LDR) system limit is shown to be -40 dB or better, which should lead to more insights into the microphysics of convective precipitation at subfreezing temperatures (e.g., hail formation, improved hydrometeor-type classification), and in winter precipitation in general (e.g., aggregation processes, rimed versus unrimed particles). In the case of the intense hailstorm, it is shown that measurement artifacts resulting from strong cross-beam gradients of reflectivity, up to 40 dB km^{-1} at 40-km range, have been greatly reduced or eliminated. Previously noted measurement artifacts with the 1994 antenna at storm tops in intense convection have been eliminated with the dual-offset antenna. The ground (mountain) clutter example shows greatly reduced returns (in terms of near-zero mean Doppler velocity areas) because of rapid falloff in the sidelobe levels with increasing elevation angle. The greatly improved antenna performance as compared with the 1994 antenna are expected to result in corresponding data quality improvements leading to more accurate measurement of rain rate and hydrometeor classification.

Corresponding author address: Prof. V. N. Bringi, Department of Electrical Engineering, Colorado State University, Fort Collins, CO 80523.
E-mail: bringi@engr.colostate.edu

DOI: 10.1175/2011JTECHA1493.1

1. Introduction

The antenna performance requirements demanded of dual-polarized weather radars are different in many respects as compared with antennas used for other applications (e.g., single target detection). This is because precipitation is a volume-distributed "target" and large gradients of reflectivity often exist across the main beam and close-in sidelobes (say, ±5 beamwidths from boresight). These cross-beam gradients of reflectivity (henceforth referred to as simply "gradients") cause errors in the measurement of polarimetric variables (e.g., see appendix C of Hubbert et al. 1998; Brunkow et al. 2000). For weather radar antennas, achieving maximum gain is not as important as having a reduced sidelobe envelope in any plane, especially the close-in sidelobes. A high degree of beam symmetry of the main lobe (defined here as −25 dB below the peak) is also desired in the patterns when the antenna is rotated about its polarization axis (see Fig. 4 below) independent of which port is excited. It follows that this requirement implies a high degree of pattern matching in any plane between the horizontal (H) and vertical (V) ports. In terms of cross-polar patterns, it is not only the on-axis performance that is important, it is also critical that the off-axis cross-polar level in any plane is as small as possible.

McCormick (1981) has given a thorough analysis of polarization errors from the viewpoint of the circular polarization basis, while Bringi and Chandrasekar (2001, their chapter 6) have used a similar formulation for the linear polarization basis (horizontal–vertical). Radar system polarization errors have been evaluated by Metcalf and Ussailis (1984). Errors in differential reflectivity (Z_{dr}) resulting from the aforementioned cross-beam gradients have been evaluated, for example, by Pointin et al. (1988), by Ryzhkov and Zrnic (1998) in the context of specific differential phase (K_{dp}), and by Rinehart and Tuttle (1982) in the context of the dual-wavelength reflectivity (DWR) ratio.

Under a recent Major Research Instrumentation (MRI) program solicitation, Colorado State University (CSU) was awarded funds to replace its prime-focus parabolic reflector antenna, obtained in 1994, with a new dual-offset Gregorian design. The main objectives of this project were to significantly improve the electrical performance of the antenna in terms of main beam symmetry (i.e., the rotational symmetry of the pattern in any plane), to establish a low sidelobe envelope in any plane, and to improve cross-polarization performance. There are two other radars that have used the dual-offset design: (i) the C-band operational weather radar [Agenzia Regionale per la Protezione Ambientale (ARPA) Friuli-Venezia Giulia, Fossalon di Grado, Italy; see Bechini et al. (2002)] and (ii) the K_a-band dual-offset Cassegrain design by the National Oceanic and Atmospheric Administration (NOAA)/Environmental Technology Laboratory (ETL; see, e.g., Reinking et al. 1997). We describe here the first application of this type of antenna technology at S band.

The CSU–University of Chicago–Illinois State Water Survey (CSU–CHILL) radar is capable of measuring the three real and three complex terms of the Hermitian polarimetric covariance matrix in real time. If the elements of the single particle backscatter matrix is the "vector" $\mathbf{\Omega} = [S_{hh}, \sqrt{2}S_{vh}, S_{vv}]$ in the linear horizontal–vertical polarization basis, then the 3×3 Hermitian covariance matrix (Tragl 1990) for an ensemble of particles is defined as $\langle \mathbf{\Omega}\mathbf{\Omega}^{T*} \rangle$, where T and the asterisk (*) are the transpose and complex conjugate, respectively, and the angled brackets denote ensemble averaging over the particle states, such as size, shape, orientation, dielectric constant, etc. Of course, when radar samples are used one can interchange time averaging with ensemble averaging by the ergodic principle.

In the CSU–CHILL configuration, there are two transmitters (H and V) and two receivers (copolar and cross polar). The transmitters are "fired" alternately with a pulse width of 1 μs and pulse repetition time (PRT) of 1 ms, with peak power of 700 kW. For H transmission, the received complex signals proportional to $[S_{hh}, S_{vh}]$ are, respectively, routed to the [copolar, cross polar] receivers. Similarly for V transmission, typically, one PRT later, the signals proportional to $[S_{vv}, S_{hv}]$ are routed again to the [copolar, cross polar] receivers. A full description of the radar circa 1999 is given in Brunkow et al. (2000). The radar system has undergone substantial upgrades since then, including a new signal processor, dual-digital receivers, and a programmable waveform generator. Further details are provided in George (2008).

In this paper, we focus on the design considerations and characteristics of the feed, orthomode transducer (OMT), and dual reflectors. This is followed by secondary copolar patterns measured in the far field using the long-range antenna testing facility at VertexRSI, and cross-polar patterns measured using a feed horn as the source antenna, which is similar in design to that used for the antenna under test (AUT) in a short-range facility. We also demonstrate, via observations in precipitation, the improvements that are realized by the new antenna that are principally related to a significantly lower system linear depolarization ratio (LDR) limit, a superior sidelobe envelope in any plane, and data quality improvements via the reduction of artifacts in the polarimetric data in regions with large cross-beam gradients. For comparative purposes, we show some selected performance improvements relative to the 1994 CSU–CHILL center-fed parabolic reflector antenna (henceforth referred to as the 1994 antenna).

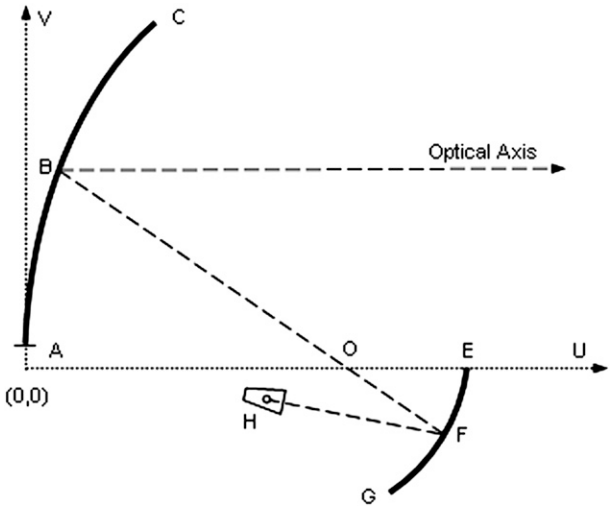

FIG. 1. Basic geometry of the dual-offset Gregorian antenna.

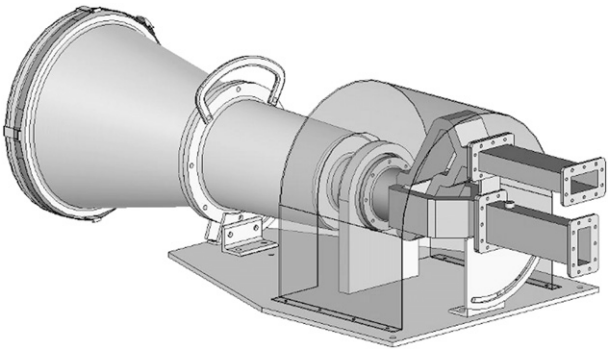

FIG. 2. Isometric view of the feed/OMT. The housing allows for rotation of the feed by 45°, effectively changing the polarization basis from nominal H–V to slant 45°–135°.

2. Design considerations

a. Description of feed/OMT

The basic dual-offset geometry (see Fig. 1) involves the feed/OMT (H), the 2-m ellipsoidal subreflector (sector EG), and the 8.5-m paraboloidal reflector (sector AC). A detailed design procedure has been given by Brown and Prata (1994). Mizugutch et al. (1976) showed that the cross-polarized component in the aperture plane resulting from the asymmetrical main reflector could be cancelled out by the asymmetrical subreflector and by a proper geometrical arrangement with the feed. This geometrical arrangement for zero cross-polar radiation in the far field is valid for geometrical optics only and is referred to as the Mizugutch condition, which has been used in our design. Of course, at microwave frequencies, where diffraction and scattering are present, the far-field cross polarization is finite. The prime focus parabolic reflector, while being inherently symmetric, suffers from aperture blockage because of feed/OMT and the support struts. While a properly designed feed (Olver et al. 1994) can achieve cross-polarization levels equivalent to a dual-offset antenna, it cannot overcome aperture blockage and its impact on sidelobe levels. In addition, symmetry is often compromised by using a ''tripod'' support strut arrangement leading to degradation in the cross-polar performance (Doviak et al. 2000).

At the outset it was decided to design a profiled corrugated horn (Olver et al. 1994). The corrugations are $\lambda/4$ in depth and the horn aperture is 3λ in diameter (the design frequency band is 2725–2875 MHz). The manufacturing tolerances for the feed were set at very ''tight'' levels that are normally used for K-band feeds. From Olver et al. (1994), the corrugation geometry controls the cross-polar patterns, the flare angle/profile controls the copolar patterns, and aperture diameter controls the copolar beamwidth. The corrugated horn supports the HE_{11} mode (H stands for hybrid; see Fig. 9.12a of Balanis 1989) as the dominant mode, which produces the desired linear fields in the horn aperture (chapter 9 of Olver et al. 1994).

A symmetric OMT (proprietary design) was chosen to achieve very high cross-polarization isolation and a very high level of port-to-port isolation. The symmetric OMT maintains a high degree of symmetry when viewed from the common square port (where the four waveguides meet; see Fig. 2, which shows an isometric view of the feed and the OMT). In particular, note the symmetry in the horizontal plane for the waveguide runs leading to the lower port (in Fig. 2), and in the vertical plane leading to upper port. The symmetric OMT was electroformed for achieving high accuracy. Table 1 lists the measured parameters of the symmetric OMT at the Torrance, California, facility over the 2.7–2.9-GHz band (swept frequency).

The feed/OMT was brought to the CSU–CHILL site for high-power testing after simulations predicted that the maximum electric field would occur in the OMT with a predicted safety margin of 22% (assuming 9-psi pressurization and 2-dB waveguide loss). The 22% predicted safety margin refers to the simulated maximum voltage versus the theoretical break-down voltage under the specified conditions. The high-power testing of the feed/OMT was successful. As mentioned earlier the nominal peak power of each transmitter is 700 kW.

TABLE 1. Measured parameters of the symmetric OMT at the Torrance facility over the 2.7–2.9-GHz band (swept frequency).

Port-to-port isolation	>58 dB
Return loss (either arm)	>24 dB
Cross-polar isolation	>43 dB

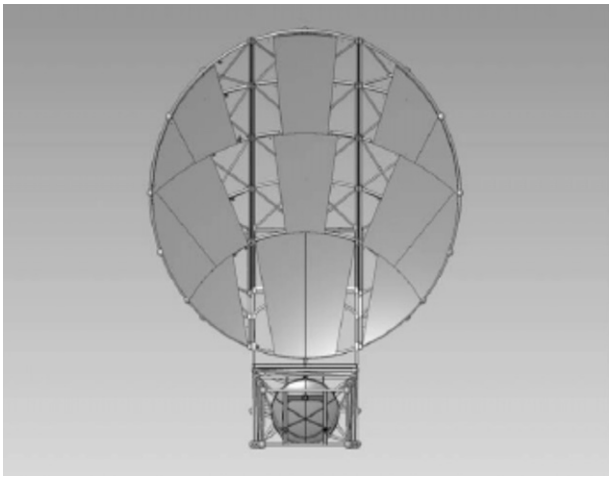

FIG. 3. Main reflector panels showing the six removable panels prior to disassembly into three sections for transport. For later reference, the antenna orientation is 0°.

b. Main reflector

The 8.5-m main reflector consists of 20 panels in three tiers as shown in Fig. 3. Each panel was made from two stretch-formed aluminum skins bonded on each side of an aluminum honeycomb core to give a very high stiffness-to-weight ratio. The surface accuracy of each panel is around 2 mil (rms; 1 mil corresponds to 0.001 in.). For disassembly and transport as per the design requirements, the reflector comes apart in three sections after six panels are removed (see Fig. 3). The 2-m ellipsoidal subreflector was constructed via a machined aluminum casting with surface accuracy of 2 mil (rms).

The far-field calculations were made with GRASP9 software (online at http://www.ticra.com). In these calculations, the theoretical first sidelobe was located very close to 1.4° off boresight. It was decided to intentionally displace the phase center of the feed 10.16 cm inward so that theoretical first sidelobe merges within the main beam (the resulting gain decreased by <0.5 dB). The feed patterns were measured in the anechoic chamber at VertexRSI. While their chamber was suitable for accurate measurements of the copolar feed patterns, there were difficulties in accurately measuring the off-axis cross-polar pattern, especially in the critical 45° plane (where the peak cross-polar levels occur). This was due to limitations of the anechoic chamber as well as the fine adjustment of the source orientation with respect to the feed under test. Hence, it was decided to use the measured E and H plane copolar feed patterns along with the measured on-axis cross-polar levels as input to GRASP9, which then models the required feed patterns needed for calculating the far-field patterns. General Dynamics SATCOM has validated this approach as being accurate for representing feed patterns and resulting far-field pattern calculations. The spherical wave function expansions (SWEs) of the modeled feed were used because near-field effects could not be ignored. Such an SWE representation of the primary feed pattern produces a more accurate calculation of the far-field sidelobes, especially those in the subreflector ''back lobe'' region (roughly 20°–40° from boresight). The surface formed by the 20 panels with gaps were used as input along with the subreflector and the geometry, as in Fig. 1. These far-field calculations (not shown here) were used to establish that the antenna satisfied the critical design review part of the contract.

3. Range tests

The completed antenna was tested at VertexRSI's long-range pattern measurement facility shown in Fig. 4. Note that the elevation angle to the flat plate on the top of the tower is 2° and the distance between source and the AUT is 4.2 km, which is well in the far field (1.5 km) for a 8.5-m reflector in our frequency band (2.7–2.9 GHz). The long-range facility was mainly used to validate the main beam symmetry and copolar sidelobe envelope specifications with patterns cut in the azimuth (with a narrow angle of ±45° and wide angle of ±180°) and elevation planes (from −1.5° to 90°) with the AUT at orientations of 0°, ±45°, and 90°.

For validation of the cross-polar pattern specifications it was decided to use the short-range test facility shown in Fig. 5 where the elevation angle to the source is close to 12° and the distance from the source to AUT is 225 m. Even though the distance is well below the far-field requirement it was judged that the cross-polar patterns would be sufficiently accurate (i.e., unlike the main beam the cross-polar pattern is not representative of a focused beam). The source feed was also a profiled corrugated horn, similar to the feed for the antenna under test, in order to minimize the cross-polarization radiated by the source (note that available standard gain horns did not meet our requirements of −40-dB cross-polar performance with the needed gain). All of the patterns were made in the elevation plane (from −2° to 10° relative to the beam center) with the AUT at orientations of 0°, ±45°, ±90°, ±135°, and 180°. The elevation plane scanning was done to minimize range effects (reflections, multipath, etc.) by pointing the main lobe at high elevation angles, which was critical for accurate cross-polar patterns off boresight.

A comprehensive range test plan was executed using both the long- and short-range test facilities with a total of more than 40 pattern cuts to fully characterize the test antenna (the final report is available from Colorado

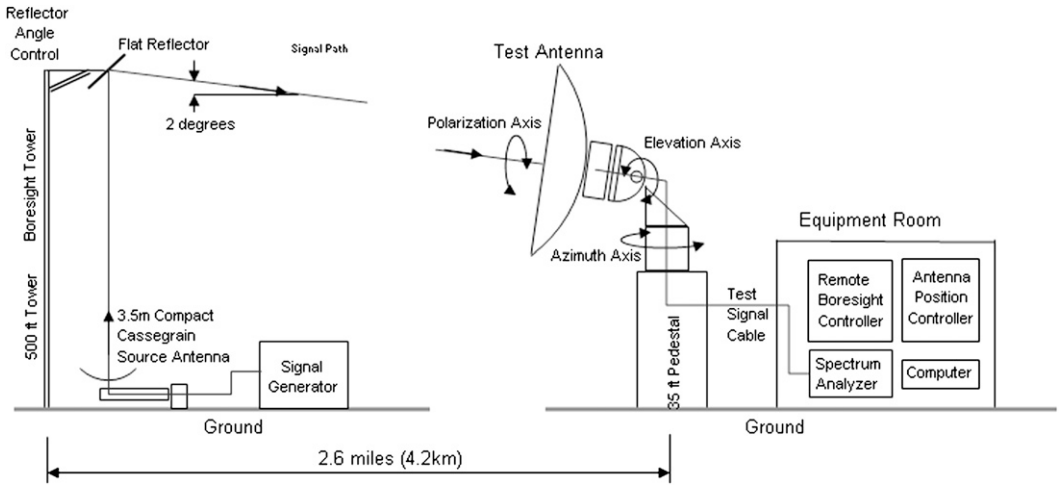

FIG. 4. Long-range test facility in Kilgore used for wide-angle azimuth patterns (mainly copolar) with test antenna at orientations of 0°, 45°, −45°, and 90°. Note that the 500-ft-high tower corresponds to 152.4 m.

State University from the corresponding author upon request). Only a few sample patterns will be shown here for illustration. First, in Fig. 6 we show a typical wide-angle pattern using the long-range facility, where the AUT orientation is 0° as in Fig. 3 [henceforth the AUT orientation is viewed facing the antenna, with positive angles corresponding to counterclockwise (CCW) rotation and vice versa]. The sidelobe envelope specification (drawn in Fig. 6) ranges from −33 dB at 2° to −50 dB at 10°, with logarithmic variation with angle (θ), and <-50 dB from 10° to 180°. Equivalently, it is expressed as

sidelobe envelope

$$= -25.7 - 24.3\log_{10}(\theta)\,\text{dB} \quad \text{for} \quad 2 < \theta < 10^\circ \tag{1a}$$

$$< -50\,\text{dB} \quad \text{for} \quad 10 < \theta < 180^\circ. \tag{1b}$$

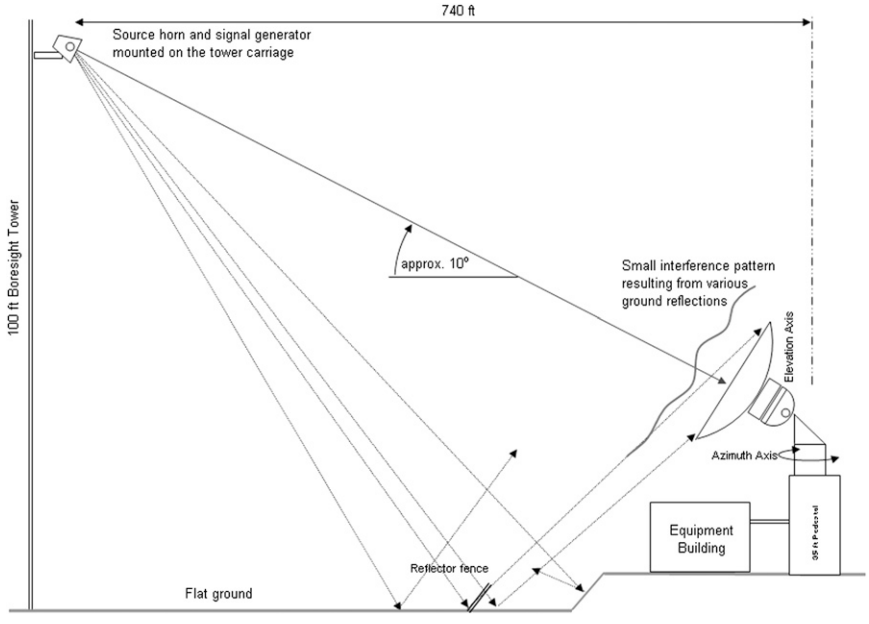

FIG. 5. Short-range test facility used mainly for narrow angle elevation patterns (cross polar). Source horn is of similar design to the feed constructed for the antenna under test. The 100-ft tower and the 740-ft distance from the source to the antenna under testing correspond to 30.5 and 225.5 m, respectively.

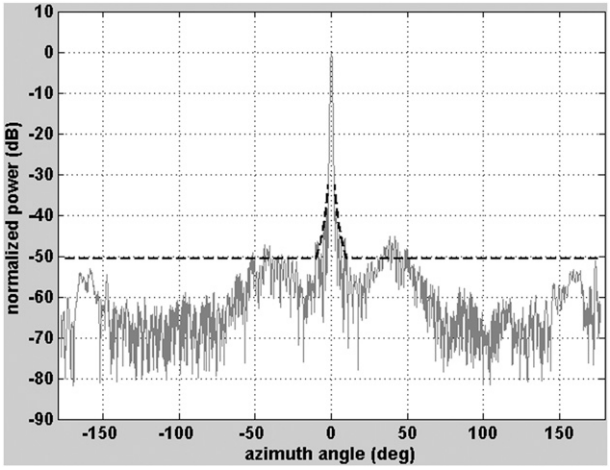

FIG. 6. Wide-angle (±175°) azimuth plane cut using the long-range facility. Source is at H polarization and AUT is at 0° orientation (as in Fig. 3), i.e., the copolar pattern. The envelope specification (dashed line) is shown.

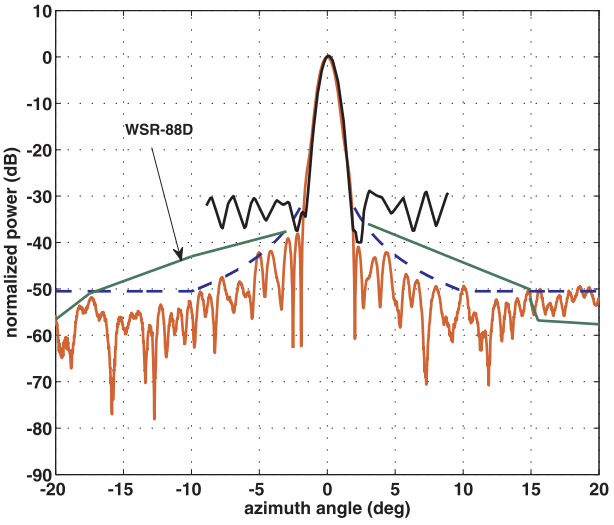

FIG. 7. Antenna patterns (copolar) as follows: dual-offset oriented at −45° (red line) and sidelobe envelope specification [blue dashed line; see Eq. (1)]; circa 1994 CSU–CHILL center-fed parabolic antenna oriented at 135° (black line); and sidelobe envelope for a WSR-88D antenna from the Paramax report (green line; D. Zrnic 2010, personal communication) in the ''best'' case plane (E-plane azimuth cut).

Local peak deviations of <2 dB above the specified envelope were allowed for $2 < \theta < 10°$, and up to 5 dB for $\theta > 10°$; the latter accommodated the subreflector ''spill over'' angular region seen in Fig. 6 for θ in the 30°–50° interval.

Figure 7 shows narrow angle patterns [−20°, 20°] comparing the dual-offset antenna (AUT at −45°) patterns with (i) the 1994 CSU–CHILL parabolic reflector antenna pattern in its ''worst'' case 135° orientation [for other planes, cf. Bringi and Chandrasekar (2001)], and (ii) the sidelobe envelope from a Weather Surveillance Radar-1988 Doppler (WSR-88D) antenna from patterns measured at Andrew Canada Inc., Andrews, Canada, as described in the Paramax report (D. Zrnic 2010, personal communication). A portion of this envelope was also shown in Fig. 2a of Doviak et al. (2000). We have selected data from the ''best'' plane (in terms of the lowest sidelobe envelope) from among the three plane cuts that are available in the above-referenced Paramax report. Note the relatively poor sidelobe performance of the 1994 CSU–CHILL antenna, which does not fall off rapidly with angle away from the boresight. This gives rise to ''ridges'' of high sidelobes in the 45°/135° planes, which contain the feed support struts and waveguide runs. Even the WSR-88D-measured sidelobe envelope (with less aperture blockage resulting from tripod feed supports) is significantly higher than the specified envelope of the dual-offset antenna. These results are not surprising because the dual-offset antenna by design eliminates all aperture blockage, giving rise to very high sidelobe performance in any plane.

We now show cross-polar patterns that are taken in the short-range facility. As mentioned before, all of the patterns were cut in the elevation plane only to avoid, as much as possible, any interference resulting from multipaths entering via the main lobe. The specifications for the cross-polar pattern were the on-axis cross-polar level <−43 dB and off axis <−35 dB for $0 < \theta < 2°$. Beyond 2°, the cross-polar level should be <−45 dB.

Figures 8a and 9 show the patterns with the AUT at orientations of −45° and −90°, respectively. The copolar pattern will be in the near field and its main lobe will ''appear'' to be wider and defocused. As can be seen, the cross-polar patterns have a minima on axis and the off-axis peaks are symmetrically placed within the angular range from −2° to 2°. Examination of the cross-polar patterns showed that the worst-case off-axis cross-polar levels occurred in the 45°/135° planes (Fig. 10 shows the antenna at the 135° position) in agreement with theory. For comparison, Fig. 8b shows the copolar and cross-polar patterns of the 1994 CSU–CHILL antenna oriented at 135° (worst-case plane) made at the manufacturer's test range. The axes scales have been arranged for easy comparison with Fig. 8a. Within the main beam the peak off-axis cross-polar level for the 1994 antenna is −32 dB while for the dual offset it is −37 dB. Moreover, beyond 2°, the cross-polar power for the dual-offset rapidly falls off to −60 dB at 3°, whereas for the 1994 antenna it stays nearly constant between −33 and −40 dB (and, in fact, comparable to the copolar sidelobe levels).

The antenna was installed on the CSU–CHILL pedestal in early 2008. After installation the photogrammetry

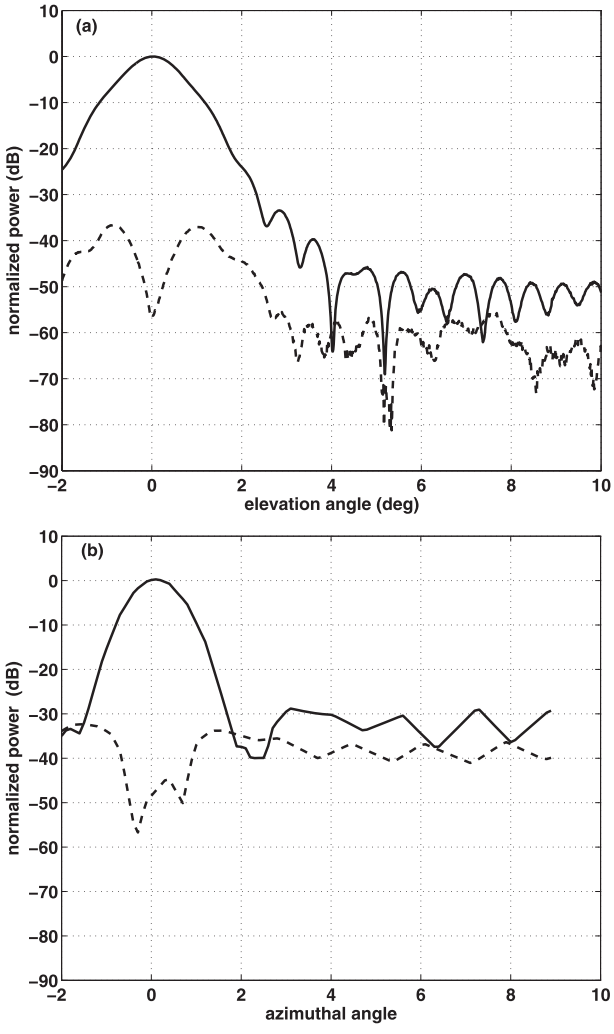

FIG. 8. (a) Elevation cut with AUT oriented at −45°. Measurements taken in the short range (see Fig. 5). The near-field copolar pattern (solid line) and the cross-polar pattern (dashed line) are shown. (b) Copolar and cross-polar patterns for the 1994 CSU–CHILL antenna in the 135° plane [same as Fig. 6.15a of Bringi and Chandrasekar (2001) except with axes limits changed for easy comparison with (a)].

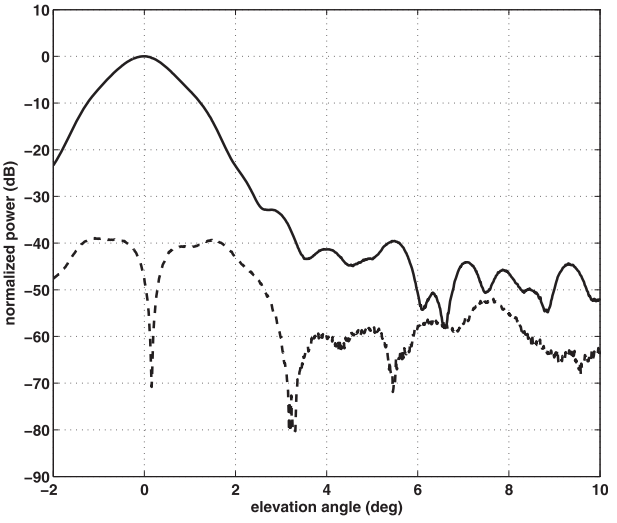

FIG. 9. As in Fig. 8a, except for AUT oriented at −90°.

method was used to establish the main reflector surface accuracy at 0.016 in. (0.4 mm) rms (as opposed to the specification of 0.02 in. or 0.5 mm), and to precisely align the geometry as per the design drawings. Table 2 lists the principal antenna characteristics/specifications.

4. Measurements

Ultimately, the antenna performance and the resultant data quality improvements of the dual-offset antenna must be determined via measurements in precipitation. Several performance measures were considered among them, including (i) the system LDR limit in light stratiform rain; (ii) the reduction in cross-beam, gradient-induced artifacts, especially in differential reflectivity (Z_{dr}), linear depolarization ratio (LDR), differential phase (Φ_{dp}), and copolar correlation coefficient (ρ_{co}); and (iii) the reduction in ground (mountain) clutter returns resulting from greatly improved sidelobe performance. Relative to (i) and (iii) we are able to compare the performance of the dual-offset with the 1994 antenna.

a. Stratiform rain

To illustrate the improvement in the quality of the LDR measurements with the dual-offset versus the 1994 antenna, data in what we consider to be ''similar'' stratiform rain are compared. Figures 11a,b show the plan position indicator (PPI) of reflectivity at 1.5° elevation angle (i) measured on 5 June 2008 with the dual offset, and (ii) measured on 18 May 2007 with the 1994 antenna. In each panel, a polar area is marked from which data were analyzed; four PPI sweeps were used to increase the number of resolution volumes used in constructing histograms of Z_h, Z_{dr}, and LDR to be shown later in Fig. 12. The CSU–CHILL radar was operated in the alternating (VH) mode with the two transmitters firing alternately with the PRT set at 1 ms. The copolar signals were routed to the copolar receiver; similarly, the cross-polar signals were routed to the second cross-polar receiver. The gate spacing used was 150 m.

Identical preprocessing steps were used to analyze the data from the two events as listed below:

- All power-related measurements were corrected for noise, assuming a constant value based on blue sky returns.

FIG. 10. Antenna at 135° position on the test range.

- A data mask has been applied to data from each beam using the standard deviation of Φ_{dp} (differential propagation phase) over 10 consecutive gates, with values $<5°$ being classified as backscatter from precipitation particles (based on Ryzhkov et al. 2005), or as backscatter of non-meteorological origin.
- The LDR system offset was determined on each day using the sun as a source to calculate the difference in receiver gains (<0.6-dB offset).
- The thresholds used for Z_h, cross-polar signal-to-noise ratio (SNR), and copolar correlation coefficient were, respectively, 10 dBZ, 10 dB, and 0.975 for constructing the histograms (the histograms were not found to be very sensitive to the precise thresholds used).

Figure 12a–c show, respectively, the histograms of Z_h, Z_{dr}, and LDR for the two events (the solid line corresponds to the dual offset and the dashed line corresponds to the 1994 antenna). Data from more than 16 000 resolution volumes (from each event) have gone into constructing the histograms. The purpose of showing the histograms of Z_h and Z_{dr} is to hypothesize that from a radar viewpoint, the two antennas were approximately observing similar stratiform rain at similar ranges and elevation angles. What is of importance here is Fig. 12c, which is where the histograms of LDR are compared. The mode of the distribution has been significantly lowered from −28 (from the 1994 antenna) to −37 dB (from dual offset). It is highly unlikely that the 9-dB lowering of the LDR mode is due to the differences in raindrop shapes or orientations in the observed events. For example, the change in LDR can be calculated (for Rayleigh scattering) using Eq. (7.40a) from Bringi and Chandrasekar (2001) using the modal Z_{dr} values from the two events (0.8 versus 0.4 dB) and assuming that the canting angle distribution is Gaussian with [0°; $\sigma = 7.5°$; see Huang et al. (2008)]. For Z_{dr} = [0.8; 0.4 dB] the corresponding calculated LDR would be [−36; −42 dB], which is in the opposite direction implied by the shift in modal LDR in Fig. 12c, that is, [−37; −28 dB]. In essence, the smaller modal Z_{dr} implies more spherical drops and thus should have given lower intrinsic LDR of around −42 dB. It follows that the 1994 antenna was incapable of measuring LDR down to these levels. We estimate from these data that the dual-offset antenna has a lower LDR system limit by 7–8 dB, as compared with the 1994 antenna.

TABLE 2. Antenna characteristics/specifications.

Type	Dual-offset Gregorian
Frequency	2725–2875 MHz
3-dB beamwidth (from measurements)	0.97° (2725 MHz) 0.93° (2875 MHz)
Gain (measured)	45.5 dB (at 2725 MHz)
Main reflector surface accuracy	0.016 in. (measured on site)
Polarization basis	H–V or slant 45°–135°
Feed	Profiled corrugated horn
Orthomode transducer	Symmetric
On-axis cross-polarization (specification)	<-43 dB
Peak off-axis cross-polarization (specification)	<-35 dB in any plane
Sidelobe envelope (specification)	-25.7–$24.3 \log_{10}(\theta)$: $2° < \theta < 10°$ <-50 dB $10° < \theta < 180°$ <-45 dB in subreflector spillover angles ~30°–50°
LDR system limit estimated from data collected in stratiform rain	−40 dB or better

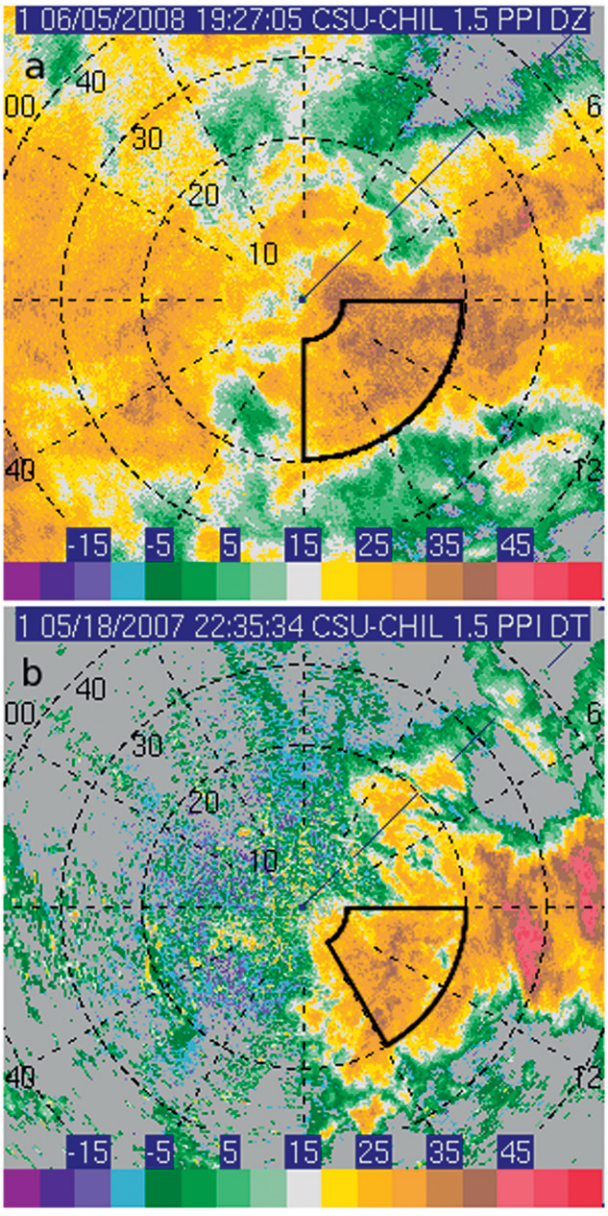

FIG. 11. PPI of reflectivity (Z_h) at 1.5° elevation angle in stratiform rain (a) using the dual-offset antenna on 5 Jun 2008, and (b) using 1994 antenna on 18 May 2007. The polar areas, from which the data were used in the histograms, are outlined in solid black for each event.

b. *Thunderstorm observations*

To illustrate the measurement accuracy achievable in regions with strong cross-beam reflectivity gradients (>20 dB km^{-1}), we show PPI scan data taken from a hailstorm that occurred at 0143:48 UTC 21 June 2008. Figure 13 shows sector scans at 1.45° elevation angle of Z_h, Z_{dr}, LDR, and Φ_{dp}. A hail signature can be noted surrounding the area near the intersection of the

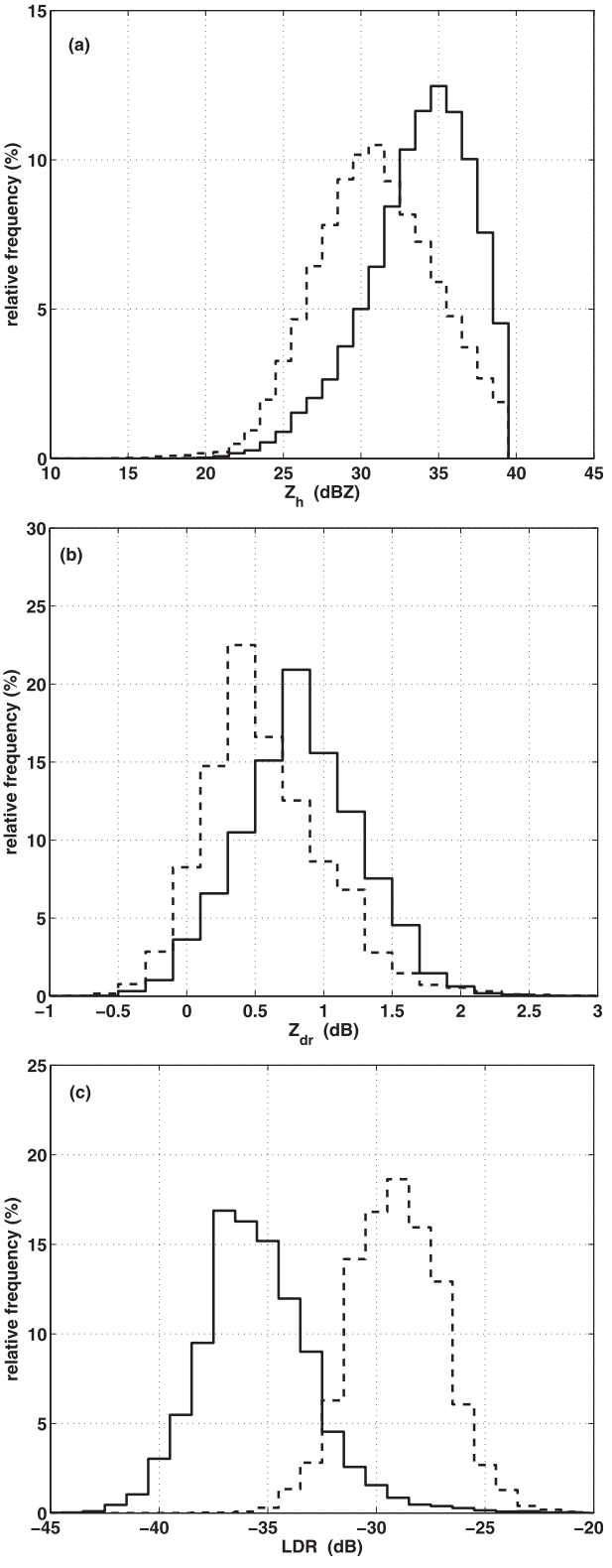

FIG. 12. Histograms of (a) reflectivity using dual-offset antenna (solid line) and 1994 antenna (dashed line), (b) Z_{dr}, and (c) LDR. The polar areas from which data were used are marked in Fig. 11. Data were taken from four PPI sweeps in each case (~17 000 resolution volumes for 5 Jun 2008, and ~16 000 for the 18 May 2007 event).

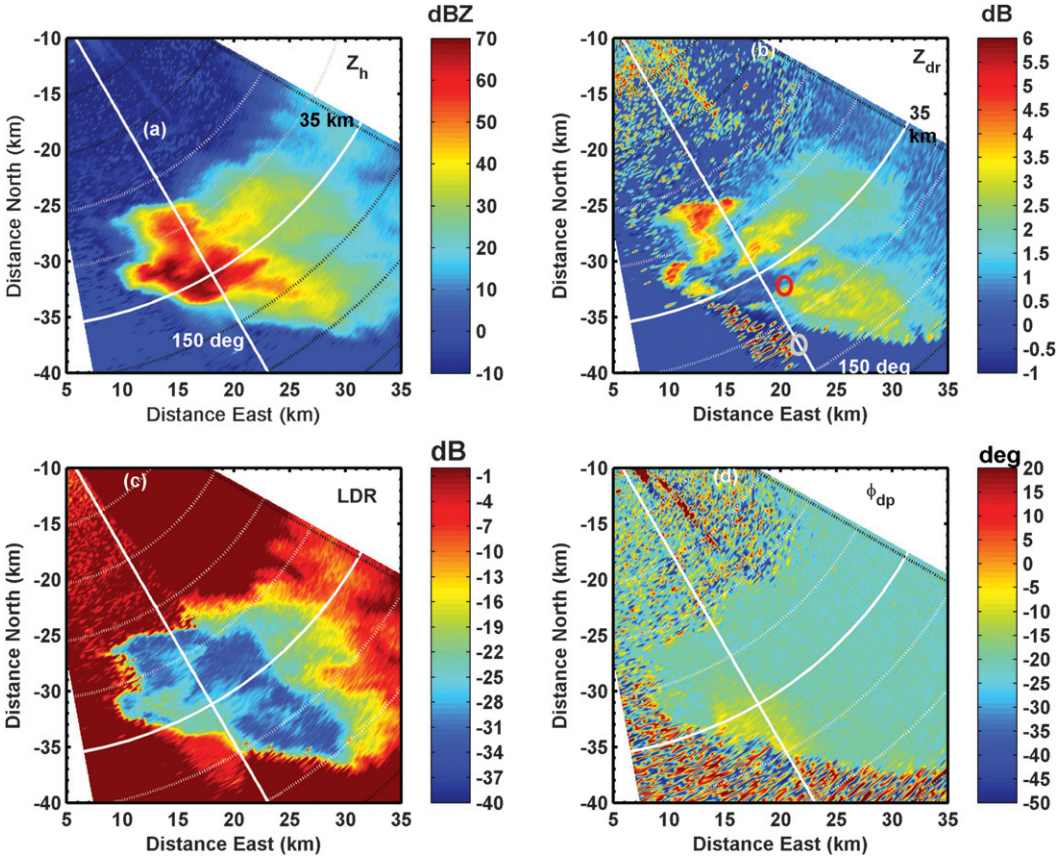

FIG. 13. Four panel set of sector PPI scan data at 1.45° elevation angle: (a) Z_h, (b) Z_{dr}, (c) LDR, and (d) Φ_{dp}. The solid white range ring is at 35 km with other dashed rings at 5-km spacing. In (b), the center of the hail (red circles) and the three-body scattering signatures (white open circles) are approximated. The solid white radial is marked at 150° along which RHI scan data are shown in Fig. 16. The radar is at the origin.

35-km-range ring and the 150° radial (high $Z_h > 60$ dBZ and low Z_{dr} in the 0–0.5-dB range marked by the open red circle in Fig. 13b), along with the distinctive three-body scattering signature [TBSS; marked by open white circle in Fig. 13b; see Zrnic (1987) and Zrnic et al. (2010)]. While the intent here is not on the interpretation of radar data in a hailstorm for which we refer to chapter 7 of Bringi and Chandrasekar (2001) and references contained therein, we focus rather on the strong cross-beam gradient present, for example, as a function of azimuth angle along the 35-km-range ring to the west of the main reflectivity core. A close examination of this region shows no obvious artifacts in Z_{dr}, LDR, or Φ_{dp} data (except for the aforementioned rather obvious distinctive TBSS, which is not related to the sidelobes). For example, at the range of 33 km (see Fig. 13b), the Z gradients are large but no Z_{dr} artifacts are noted.

To make a more quantitative assessment, Fig. 14 shows Z_h and Z_{dr} as a function of azimuth angle along the 35-km-range ring. Between azimuth angles of 155° and 160°, the slope of Z_h is marked (20 and 38 dB km^{-1}). While noting that the measured Z_h is smoothed by the antenna main beam (and that the true gradients are likely to be larger), there appears to be no obvious Z_{dr} artifact signatures between 140° and 160°. The only artifact signature appears at an azimuth angle of 164° (with a peak Z_{dr} of 4.5 dB), which is likely due to the TBSS (see, also, the Z_{dr} image in Fig. 13b along the 35-km-range ring at the western edge of the main reflectivity core). In Fig. 15, the cross-polar SNR (dB) and LDR are shown as functions of the azimuth angle. The noticeable feature here in the strong gradient region between 155° and 160° and the gradual increase in LDR from −30 dB at 157.5° to 0 dB at 160°. Beyond that the LDR is not calculated. The increase in LDR is due to the cross-polar power not being adequately corrected for system noise (see the first bullet point in section 4a). Similar examinations of Φ_{dp} and ρ_{co} versus azimuth angle do not exhibit any artifacts within the high-gradient region (not shown here).

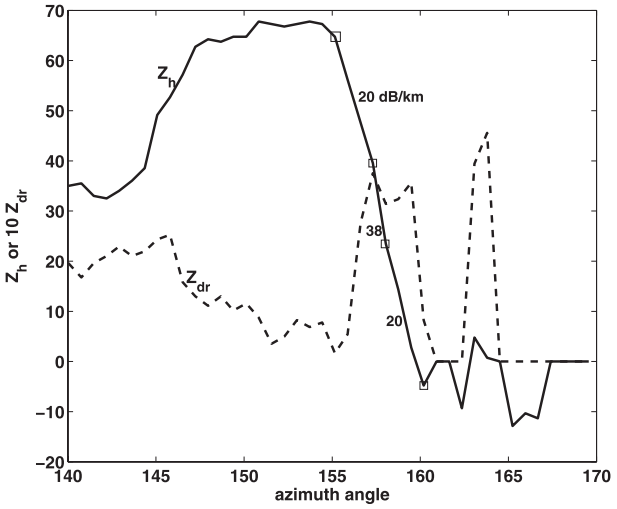

FIG. 14. Z_h and $10Z_{dr}$ as a function of azimuth angle along the 35-km-range ring marked in Fig. 13a. The slope of Z_h is noted between the open square markers as 20, 38, and 20 dB km^{-1}.

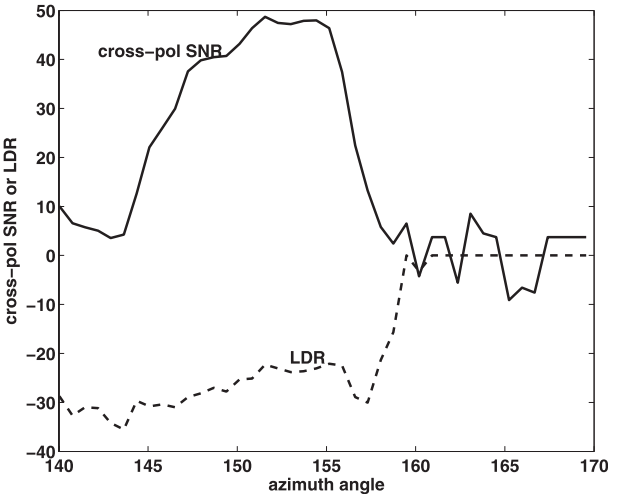

FIG. 15. As in Fig. 14, but for cross-polar SNR and LDR vs azimuth angle.

RHI scans were taken along the 150° azimuth about 3 min after the PPI scans. Figure 16 shows Z_h, mean Doppler velocity, Z_{dr}, LDR, and ρ_{co}. The reflectivity and mean Doppler velocity at storm top are seen to be exceptionally free of any gradient-induced sidelobe artifacts. Above the radar-detected top, the mean Doppler velocity is assigned a random number in the Nyquist interval (from -26 to 26 m s^{-1} in this case) because noise dominates the signal. Of interest is the feature near the storm top above the storm core at 35-km range. As one moves beyond 30 km in range, the radial velocity is positive (denoted in yellow, indicating that particles are moving with radial component of velocity away from the radar), and as one proceeds in range, the radial velocity hits the Nyquist boundary and the velocity abruptly changes (i.e., aliases) from +26 m s^{-1} (red) to -26 m s^{-1} (very dark blue). The actual radial velocity at storm top at 40-km range is close to +31 m s^{-1}, implying strong divergence above the storm core.

The polarimetric variables are also shown in Fig. 16. Apparent Z_{dr} artifacts are restricted to a small, low-SNR area near $x = 43$, $z = 7$ km. The hail shaft at 32-km range and the large drop in Z_{dr} signatures around it are clearly visible. The LDR image also reflects the exceptional performance of the dual-offset antenna with values < -35 dB being frequently observed aloft. At storm edges the gradual increase in LDR is due to the inadequate correction of noise power when the cross-polar SNR decreases. The TBSS is visible at ($x = 40$, $z = 2$ km). The hail shaft at 32 km and the melting level are clearly demarcated near 2–2.5-km height. Because of the enhanced dynamic range of LDR with the new antenna, we are now able to discern subtle changes in LDR in the ice region aloft, which have not been hitherto observed.

The RHI of the copolar correlation is shown as the last panel in Fig. 16, except that $1 - \rho_{co}$ is plotted to show the deviation from unity with higher resolution. Except for the region near ($x = 40$, $z = 7$ km) and perhaps within the TBSS (at 38-km range near 1–1.5-km height), the copolar correlation coefficient field is remarkably uniform (>0.99) above the melting level. The hail shaft itself is clearly demarcated by significant lowering of ρ_{co} to values around 0.94. There are also discernible variations near the melting level (2–2.5-km height). Overall, the quality of the reflectivity, mean Doppler velocity, and the polarimetric variables is as such, inferred to reflect the very high quality of the antenna.

c. *Clutter observations with the two antennas*

Because of the low sidelobe levels achieved by the dual-offset antenna, ground clutter contamination decreases rapidly with increasing antenna elevation angle. In anticipation of the installation of the new antenna, a series of low-elevation-angle PPI scans were done shortly before the 1994 center-fed parabolic antenna was removed from service in June 2007. The radar was operated in single-polarization (H only) mode. These same scans were repeated in June 2008 with the new antenna. In both cases, the data were collected with the same system parameters (e.g., elevation angles, PRT, scan rate, clutter filter off, etc.) and under well-mixed afternoon conditions when normal beam propagation was

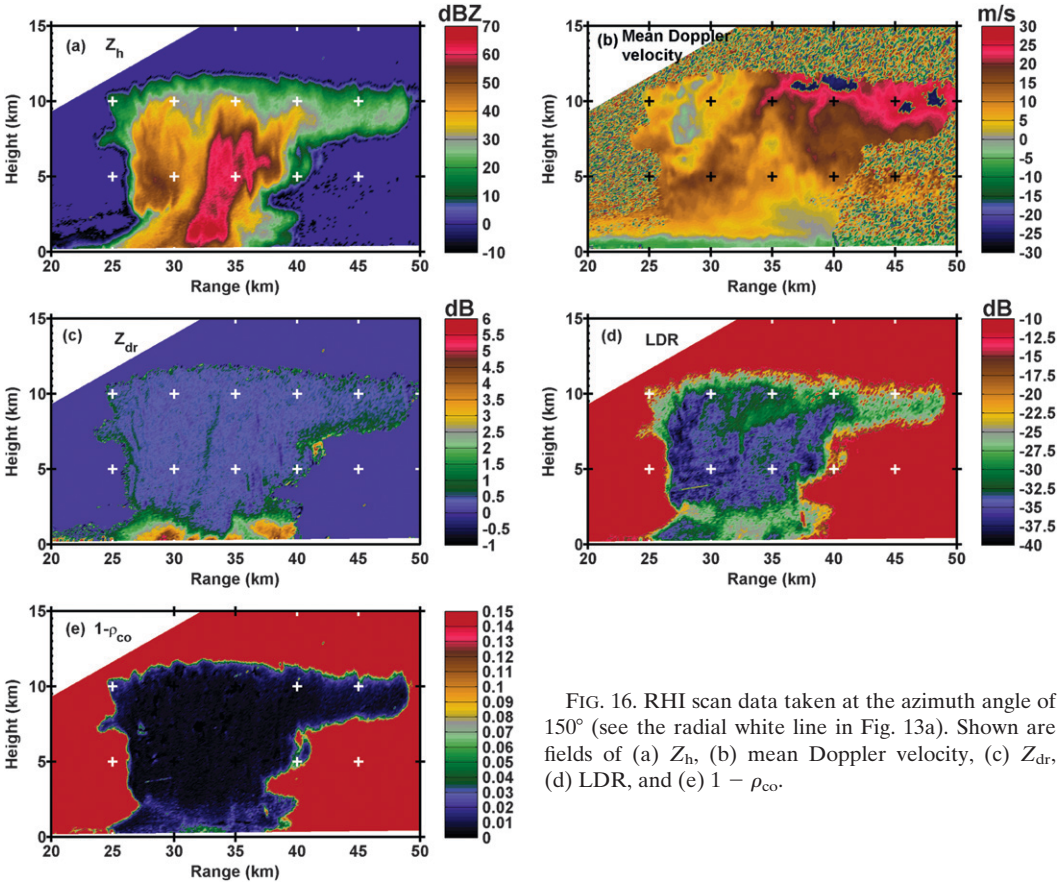

FIG. 16. RHI scan data taken at the azimuth angle of 150° (see the radial white line in Fig. 13a). Shown are fields of (a) Z_h, (b) mean Doppler velocity, (c) Z_{dr}, (d) LDR, and (e) $1 - \rho_{co}$.

expected. Figure 17 shows the radial velocity patterns obtained with the two different antennas (Fig. 17a corresponds to the dual offset and Fig. 17b corresponds to the center-fed offset). In both plots, gates where the normalized first lagged autocorrelation magnitude was less than 0.3 were taken to be noise and removed (Keeler and Passarelli 1990). At an elevation angle of 3.5°, the main beam axis just clears the highest elevation terrain in the Rocky Mountains (centered approximately 80 km west of the radar). The sidelobe levels of the 1994 antenna cause detectable clutter return (as indicated by mean Doppler velocity, which is essentially 0) to appear over much of the high terrain area (Fig. 17b). Because of the suppressed sidelobe illumination generated by the dual-offset antenna, minimal ground clutter return is seen in the data collected with the dual-offset antenna (Fig. 17a).

5. Summary

The quality of data from a polarimetric Doppler radar is strongly dependent on the electrical performance of the antenna. Most weather radars use the center-fed parabolic reflector. Even with a high-quality feed/OMT, the blockage caused by feed support struts and waveguide runs deteriorates the sidelobe performance, especially in the planes containing (and orthogonal to) the feed support struts. A dual-offset design as presented in this paper eliminates any blockage in the aperture plane leading to excellent sidelobe performance in any plane. The cross-polarized component in the aperture plane resulting from the asymmetrical main reflector is cancelled out by the asymmetrical subreflector and by a proper geometrical arrangement with the feed (Mizugutch et al. 1976). This latter arrangement, along with a profiled corrugated horn and symmetric OMT, allows for exceptional cross-polar performance leading to an LDR system limit of −40 dB or better.

We have discussed some aspects of the antenna and feed/OMT design that has led to a very high performance antenna that was designed and custom built for a weather radar at S band. We have shown examples of data quality improvements using data collected in light and intense precipitation, and the reduction of returns from mountain clutter. In particular, data quality in

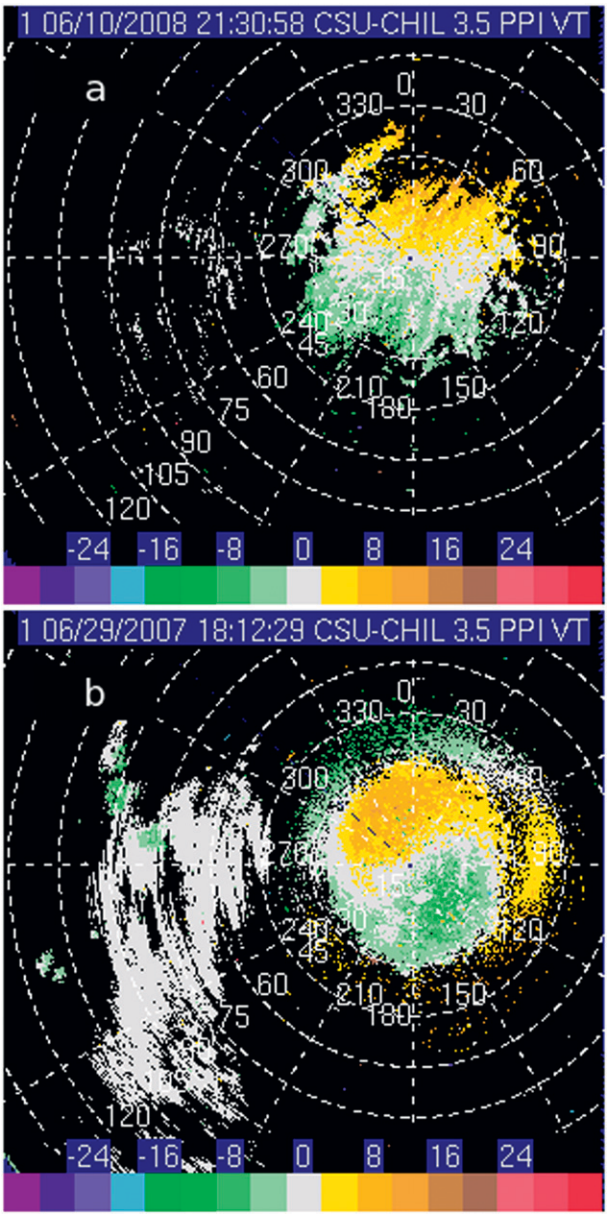

FIG. 17. PPI sweep of mean Doppler velocity (m s^{-1}) taken at elevation angle of 3.5° to illustrate reduction in area of returns with near 0 mean Doppler velocity (from mountain clutter) taken with (a) dual offset compared with (b) 1994 antenna.

strong reflectivity gradients are shown to be free of artifacts commonly found when using the circa 1994 CSU–CHILL parabolic reflector antenna. From data in a severe hailstorm, it is estimated that cross-beam gradients as large as 40 dB km^{-1} can be tolerated at ranges <40 km without significant measurement artifacts. With the 1994 parabolic reflector antenna the maximum tolerable gradients were around 20 dB km^{-1} at similar ranges (Hubbert et al. 1998).

Acknowledgments. The CSU–CHILL National Radar facility is supported by the National Science Foundation under ATM 0735110 and the Colorado State University. The new antenna acquisition was made possible by a Major Research Instrumentation grant from the U.S. National Science Foundation (NSF) via ATM 0216192. General Dynamics SATCOM provided cost-sharing funds of 15% for design and range testing. CSU is grateful to Dr. P. Ramanujam for his contributions during the preliminary and critical design reviews.

Dr. Raj Chugh was instrumental in the RF design of the very low cross-polarization dual-offset antenna system described in this paper. Sadly, near the end of the project, he passed away at the age of 58 on 23 May 2005, yet will be remembered by all involved. Rajinder Kumar Chugh was born in District Kamaliya Layalpur, Pakistan, on 2 November 1946. He received his BEE from the Indian Institute of Technology (IIT) in New Delhi, and then his Ph.D. in electromagnetics at the University of Manitoba in Canada. After several professional adventures, he came to Vertex Communications Corporation (now General Dynamics) in 1984 as Principal Scientist. Raj's understanding and computational carefulness were his highly recognized trademarks; everything was always correct.

REFERENCES

Balanis, C. A., 1989: *Advanced Engineering Electromagnetics*. John Wiley and Sons, 981 pp.

Bechini, R., E. Gorgucci, G. Scarchilli, and S. Dietrich, 2002: The operational weather radar of Fossalon di Grado (Gorizia, Italy): Accuracy of reflectivity and differential reflectivity measurements. *Meteor. Atmos. Phys.,* **79,** 275–284.

Bringi, V. N., and V. Chandrasekar, 2001: *Polarimetric Doppler Weather Radar*. Cambridge University Press, 636 pp.

Brown, K. W., and A. Prata, 1994: A design procedure for classical offset dual reflector antennas with circular apertures. *Trans. IEEE Antennas Propag.,* **42,** 1145–1153.

Brunkow, D., V. N. Bringi, P. C. Kennedy, S. A. Rutledge, V. Chandrasekar, E. A. Mueller, and R. K. Bowie, 2000: A description of the CSU–CHILL National Radar Facility. *J. Atmos. Oceanic Technol.,* **17,** 1596–1608.

Doviak, R. J., V. Bringi, A. Ryzhkov, A. Zahrai, and D. Zrnic, 2000: Considerations for polarimetric upgrades to operational WSR-88D radars. *J. Atmos. Oceanic Technol.,* **17,** 257–278.

George, J., 2008: Transformation of CSU-CHILL into a virtual radar system. M.S. thesis, Dept. of Electrical and Computer Engineering, Colorado State University, 202 pp.

Huang, G.-J., V. N. Bringi, and M. Thurai, 2008: Orientation angle distributions of drops after 80 m fall using a 2D-video disdrometer. *J. Atmos. Oceanic Technol.,* **25,** 1717–1723.

Hubbert, J., V. N. Bringi, L. D. Carey, and S. Bolen, 1998: CSU–CHILL polarimetric radar measurements from a severe hail storm in eastern Colorado. *J. Appl. Meteor.,* **37,** 749–775.

Keeler, R. J., and R. E. Passarelli, 1990: Signal processing for atmospheric radars. *Radar in Meteorology: Battan Memorial and*

40th Anniversary Radar Meteorology Conference, D. Atlas, Ed., Amer. Meteor. Soc., 199–229.

McCormick, G. C., 1981: Polarization errors in a two-channel system. *Radio Sci.,* **16,** 67–75.

Metcalf, J. I., and J. S. Ussailis, 1984: Radar system errors in polarization diversity measurements. *J. Atmos. Oceanic Technol.,* **1,** 105–114.

Mizugutch, Y., M. Akagawa, and H. Yokoi, 1976: Offset dual reflector antenna. *Proc. 14th Antennas and Propagation Society Int. Symp.*, Amherst, MA, IEEE, 2–5.

Olver, A. D., P. J. B. Clarricoats, A. A. Kishk, and L. Shafai, 1994: *Microwave Horns and Feeds*. IEE Electromagnetic Waves Series, Vol. 39, IEE UK and IEEE New York, 490 pp.

Pointin, Y., D. Ramond, and J. Fournet-Fayard, 1988: Radar differential reflectivity Z_{DR}: A real-case evaluation of errors induced by antenna characteristics. *J. Atmos. Oceanic Technol.,* **15,** 416–423.

Reinking, R. F., S. Y. Matrosov, R. T. Bruintjes, and B. E. Martner, 1997: Identification of hydrometeors with elliptical and linear polarization K_a-band radar. *J. Appl. Meteor.,* **36,** 322–339.

Rinehart, R. E., and J. D. Tuttle, 1982: Antenna beam patterns and dual-wavelength processing. *J. Appl. Meteor.,* **21,** 1865–1880.

Ryzhkov, A., and D. Zrnic, 1998: Beamwidth effects on the differential phase measurements of rain. *J. Atmos. Oceanic Technol.,* **15,** 624–634.

——, T. J. Schuur, D. W. Burgess, P. L. Heinselman, S. E. Giangrande, and D. S. Zrnic, 2005: The Joint Polarization Experiment. *Bull. Amer. Meteor. Soc.,* **86,** 809–824.

Tragl, K., 1990: Polarimetric radar backscattering from reciprocal random targets. *IEEE Trans. Geosci. Remote Sens.,* **8,** 856–864.

Zrnic, D. S., 1987: Three-body scattering produces precipitation signatures of special diagnostic value. *Radio Sci.,* **22,** 76–86.

——, G. Zhang, V. Melnikov, and J. Andric, 2010: Three-body scattering and hail size. *J. Appl. Meteor. Climatol.,* **49,** 687–700.